



Distribution of relaxation times-based analysis of aging mechanisms and prediction of heating domain for alternating current pulse self-heating lithium-ion batteries

Zixian Zhuang^a, Jun Li^a, Weiling Luan^{a,*}, Haofeng Chen^{a,b,**}, Qiu-An Huang^c, Jiujun Zhang^c, Shan-tung Tu^a

^a Key Laboratory of Advanced Battery Systems and Safety (CPCIF), School of Mechanical and Power Engineering, East China University of Science and Technology, Shanghai, 200237, China

^b Department of Mechanical & Aerospace Engineering, University of Strathclyde, Glasgow, G1 1XJ, UK

^c Institute for Sustainable Energy/College of Sciences, Shanghai University, Shanghai, 200444, China

HIGHLIGHTS

- Deep analysis into aging mechanism of batteries under AC self-heating by DRT method.
- Relationship established between SEI impedance, lithium plating and battery aging.
- AC pulse selected with high amplitude and frequency to reduce the battery impedance.
- Optimal heating domain derived by the degradation mechanism based ETC model.

ARTICLE INFO

Keywords:

Lithium-ion battery
Self-heating
AC impedance
DRT
Aging mechanism
Heating domain

ABSTRACT

Lithium-ion batteries (LIBs)-based electric vehicles (EVs) often encounter challenges such as the reduction in endurance mileage and the increase in charging time at low temperatures. To address these issues, the alternating current (AC) pulse self-heating in LIBs emerges as a pivotal method to overcome performance limitations of EVs at low temperatures. However, employing AC pulsing with high amplitude and low frequency can potentially lead to battery degradation. In this study, the state transitions and aging causes of LIBs during the self-heating are meticulously examined using the distribution of relaxation times (DRT) method. The results reveal that at an AC frequency of 50 Hz or higher, even with amplitudes up to 12 C, there is no degradation for the battery used in this study. For aged LIBs, the significant rise in impedance of solid electrolyte interphase (SEI) due to lithium plating, is the main factor driving battery aging during AC self-heating. Subsequently, an electrochemical-thermal coupling (ETC) model grounded in the degradation mechanism has been developed and experimentally validated to accurately predict the optimal heating domain for self-heating. This approach holds significant implications for the rapid selection of self-heating parameters for facilitating efficient battery performance enhancement.

1. Introduction

Lithium-ion batteries (LIBs) with superior energy/power densities, and cycle-life have been widely adopted in the applications of portable electronics, electric vehicles, and stationary power stations [1–4].

However, performance of LIBs is significantly affected by cold climates [5]. In the operation of a LIB at low temperatures, the electrolyte conductivity is decreased due to the decreased ion diffusion [6,7], and the electrode overpotentials are also increased [8], resulting in decreased performance in terms of the reduced energy/power densities, and decreased cycle-life. The current battery thermal management system

* Corresponding author.

** Corresponding author. Key Laboratory of Advanced Battery Systems and Safety (CPCIF), School of Mechanical and Power Engineering, East China University of Science and Technology, Shanghai, 200237, China.

E-mail addresses: luan@ecust.edu.cn (W. Luan), haofeng.chen@ecust.edu.cn (H. Chen).

Nomenclature	
Symbols	
A	Specific surface area (m^{-1})
C_{dl}	Double layer capacitance ($\text{F}\cdot\text{m}^{-2}$)
E_a	Activation energy ($\text{kJ}\cdot\text{mol}^{-1}$)
F	Faraday's constant ($\text{C}\cdot\text{mol}^{-1}$)
R	Gas constant ($\text{J}\cdot\text{mol}^{-1}\cdot\text{K}^{-1}$)
R_{Arrhe}	Temperature correction coefficient
R_c	Contact impedance (Ω)
R_{ct}	Charge transfer reaction impedance (Ω)
R_o	Ohmic impedance (Ω)
R_{sei}	SEI impedance (Ω)
T	Battery temperature (K)
T_{env}	Environmental temperature (K)
T_r	Reference temperature (K)
Z_{Im}	Imaginary part of impedance (Ω)
Z_{Re}	Real part of impedance (Ω)
Z_{tr}	Impedance at f_{tr} (Ω)
c_e	Lithium ion concentration in the electrolyte ($\text{mol}\cdot\text{m}^{-3}$)
c_p	Specific heat capacity ($\text{J}\cdot\text{kg}^{-1}\cdot\text{K}^{-1}$)
f_{max}	Frequency at which reactance is maximum value in the mid-frequency region (Hz)
f_{tr}	Transition frequency (Hz)
h	Convective heat transfer coefficient ($\text{W}\cdot\text{m}^{-2}\cdot\text{K}^{-1}$)
j_{dl}	Current density of double layer ($\text{mol}\cdot\text{m}^{-2}\cdot\text{s}^{-1}$)
j_f	Faraday current density ($\text{mol}\cdot\text{m}^{-2}\cdot\text{s}^{-1}$)
j_i	Current density for lithium ion intercalation/deintercalation reaction ($\text{mol}\cdot\text{m}^{-2}\cdot\text{s}^{-1}$)
j_{nf}	non-Faraday current density ($\text{mol}\cdot\text{m}^{-2}\cdot\text{s}^{-1}$)
j_p	Current density of lithium plating ($\text{mol}\cdot\text{m}^{-2}\cdot\text{s}^{-1}$)
j_s	Total local current density ($\text{mol}\cdot\text{m}^{-2}\cdot\text{s}^{-1}$)
k_p	Reaction rate constant of lithium plating ($\text{m}\cdot\text{s}^{-1}$)
q_J	Total heat source ($\text{W}\cdot\text{m}^{-3}$)
ΔR_{sei}	Relative variations of R_{sei} (Ω)
ϕ_{dl}	Double layer potential (V)
ϕ_p	Reaction overpotential of lithium plating (V)
α_p	Anode transfer coefficient
ρ	Battery density ($\text{kg}\cdot\text{m}^{-3}$)
Abbreviations	
AC	Alternating Current
BTMS	Battery Thermal Management System
CC	Constant current
CV	Constant voltage
DC	Direct Current
DRT	Distribution of Relaxation Times
EDS	Energy Dispersive Spectrometer
EIS	Electrochemical Impedance Spectroscopy
ETC	Electrochemical-Thermal Coupling
EVs	Electric Vehicles
LFP	LiFePO_4
LIBs	Lithium-Ion Batteries
P2D	Pseudo-Two Dimensional
PTC	Positive Temperature Coefficient
SEI	Solid Electrolyte Interphase
SEM	Scanning Electron Microscope
SOC	State of Charge
SOH	State of Health
SSR	Sum of Squared Residuals

(BTMS) mainly aims to decrease battery temperature [9–12]. However, to overcome the challenge of battery operation at low temperatures, it is necessary to consider battery heating methods in BTMS. Currently, some external heating methods like plate heating, tube heating, positive temperature coefficient (PTC) heating, and metal-film heating, etc. [13, 14], have been developed. However, they suffer from longer heating times, lower efficiency, and uneven temperature distribution [15]. In this regard, the use of internal heating methods including low-temperature self-heating technology to preheat the LIB to an appropriate temperature range before operation seem particularly necessity and also crucial.

As recognized, the internal self-heating technologies utilizing direct current (DC) or alternating current (AC) can offer rapid heating, uniform temperature distribution, and reduced thermal loss. DC methods, such as constant current (CC) or constant voltage (CV) discharge and “all-climate battery” technologies [16], are fast but less energy-efficient and undesired acceleration of battery aging; while AC self-heating methods, such as sine [17] and pulse [18,19] waveforms, can offer better energy efficiency, temperature uniformity, and reduced aging, showing broader development prospects. Some studies have analyzed AC self-heating in batteries through experimental and simulation methods [20–22]. Researches have shown that the use of high amplitude and low frequency AC can effectively improve the heating rate of batteries in low-temperature environments. Batteries exhibit a significant temperature rise effect under high amplitude and low frequency AC conditions. Specifically, the real part of battery impedance increases at low current frequencies, therefore, according to Joule's Law, higher current amplitude and lower frequency contribute to the accumulation of heat inside the battery, thereby accelerating temperature rise. However, although this heating method can increase battery temperature effectively, it may also increase the risk of battery degeneration, especially in the case of continuous operation at higher amplitudes and lower frequencies, where

the rate of battery degradation may accelerate.

Current research on AC self-heating methods in LIBs primarily focuses on methodic strategy optimization to avoid battery degradation, but the in-depth analysis of aging causes especially induced by AC pulse cycles have rarely discussed. The currently popular and non-destructive quantitative analysis method is electrochemical impedance spectroscopy (EIS), which is the most commonly used technique for studying the dynamic characteristics of lithium-ion batteries and can explain the degradation mechanism of the battery [23]. EIS is also an effective method for determining the evolution of material dynamic behavior, such as supercapacitors, corrosion, and fuel cells [24,25]. It allows for sensitive and individual analysis of the kinetics of each electrochemical reaction process without introducing interference or causing sample damage [26], making it a precise and reliable analytical method.

In general, EIS data analysis to obtain the performance and degradation information of the LIBs has some challenges due to the overlapping of the reaction processes within the measured system. In EIS data analysis, the distribution of relaxation times (DRT) method as an alternative model-free approach does not require specific equivalent circuits to reducing the need for prior assumptions in electrochemical system studies has been identified to be feasible and efficient. Such a DRT method can offer a novel and rapid way to visually interpret impedance spectra and distinguish time constants representing individual processes in electrochemical systems, thereby revealing more information about battery internal behavior [27]. For instance, many studies have observed the presence of contact resistance in high-frequency impedance analyzes for batteries through the DRT deconvolution [28]. Currently, the DRT method is widely applied in the field of new energy, including various battery mechanisms [29,30], material evaluation [31], and prediction of battery state [32].

This study developed an AC pulse self-heating method with faster heating rate, which shows more convenience to operate compared to the

Table 1
Battery specifications.

Parameter (unit)	Value
Weight (g)	42
Size (mm)	Diameter: 18.3 Height: 65
Rated voltage (V)	3.2
Cathode and anode materials	LiFePO ₄ /Graphite
Electrolyte materials	LiPF ₆ /EC + EMC (3:7)
Maximum discharge ratio (C)/Current (A)	20/24
Capacity (mAh)	1155~1160
Operating temperature range (°C)	-20~60

Table 2
The number and name of batteries used in the experiment.

Number of batteries	Experimental Purposes	Name
1	One of the fresh batteries in the same batch	Cell 1
18	Batteries for different experimental conditions	x C x Hz battery
16	Used for temperature rise boundary finding	-
20	Used for aging boundary finding	-

sinusoidal AC heating. The temperature rise boundary of AC pulse heating is determined with emphasis on the analysis of battery aging mechanism using DRT method. For further enhancing the practical application of the presented theory in this work, an electrochemical-thermal coupling (ETC) model is established based on the analysis of the battery aging mechanism. Unlike the equivalent circuit model, the ETC model [33–35] quantitatively elucidates the relationship between AC pulse parameters and capacity degradation. Through this model, an optimal heating domain is calculated, which can satisfy the requirement for temperature rise while avoiding battery aging. This work will provide significant guidance for the implementation of AC pulse self-heating strategy in LIBs under low-temperature operation conditions.

The paper is structured as follows: Section 2 presents a comprehensive overview of the experimental design; Section 3 is divided into three subsections: Section 3.1 outlines the influence of AC parameters on temperature rise for self-heating, Section 3.2 delves into the battery aging mechanism employing the DRT method, and Section 3.3 establishes a self-heating model based on aging mechanism and determines the optimal heating domain for AC pulse self-heating by the model. Finally, Section 4 provides the research's concluding remarks.

2. Experimental

2.1. Batteries and testing platforms

In this paper, a commercial 18650 graphite||LiFePO₄ (LFP) battery was used as the example battery system. As shown in Table 1, this battery is primarily designed for high-power applications, supporting rapid discharge with high current. It has a nominal capacity of 1200 mAh, and the cutoff voltages for charging and discharging are 3.65 V and 2 V, respectively. Table 2 presents the number and names of the batteries used in the experiments with all test batteries originating from the same production batch.

The experimental setup established is illustrated in Fig. S1. (1) Bipolar power supply: a KIKUSUI PBZ20-20 (voltage range: ±20 V, current range: ±20 A, frequency range: 0.01 Hz to 100 kHz) is used to provide an AC pulse. It is controlled by a supervisory computer 1, which sets the self-heating program and records the effective values of voltage and current; (2) low-temperature environment simulation: a DGBELL BTH-150 temperature and humidity test chamber (temperature range: 40 to 150 °C, temperature fluctuation: ±0.5 °C) is utilized to create the required low-temperature environment; (3) voltage signal acquisition: the AC voltage signals across the battery are captured using a RIGOL DS1102Z-E oscilloscope (bandwidth 100 MHz, sampling rate 1 GSa/s); (4) temperature monitoring: the surface temperature of the battery is monitored using a T-type ultra-fine thermocouple (wire diameter: 0.254 mm, accuracy: 0.2 °C) with the data being recorded in a Shenhua MT-32 channel temperature recorder; (5) charge-discharge experiment: a NEWARE CT-4008Q-5V12A-S1 (accuracy: 0.01 % FS) is used to conduct the experiments with step settings and data collection completed by a supervisory computer 2; and (6) EIS testing: the EIS data of the battery under different temperatures and aging processes are measured using a Metrohm Autolab electrochemical workstation.

2.2. Temperature rise tests

To mitigate the performance degradation of LIBs under low-temperature conditions, this work employed an AC pulse self-heating method to preheating the battery to its normal operating temperature range (above 0 °C) before startup. The self-heating temperature range was set from -20 °C to 0 °C, and the State of Charge (SOC) of battery was maintained at 50 % for the experiments. Considering the time constraint before the startup of a LIBs-based electric vehicle and the time required to reach 0 °C using the AC pulse heating method, a self-heating duration of 5 min was determined. Supplementary Fig. S2 records the Nyquist plots of a fresh battery Cell 1 at various temperatures (5 °C intervals). As shown in Fig. 1, during the frequency variation, the real part of the battery impedance exhibits a distinct trend of “rapid decline followed by gradual stabilization”. At 1000 Hz, the sensitivity of the real

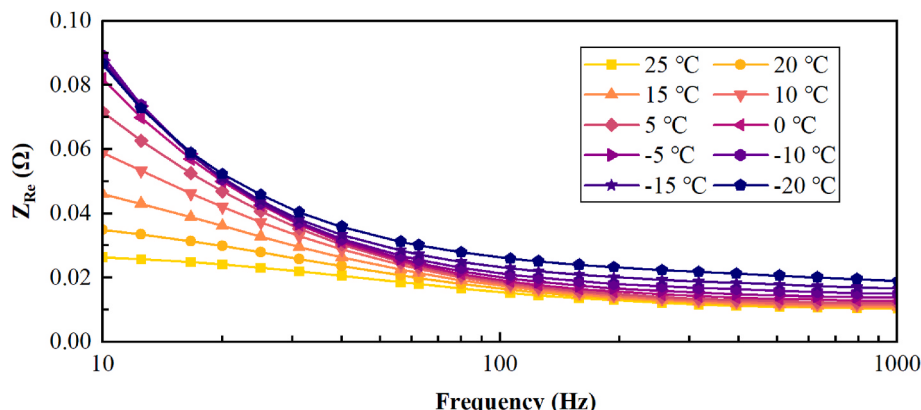


Fig. 1. The real part of the battery impedance vs. frequency under different temperatures.

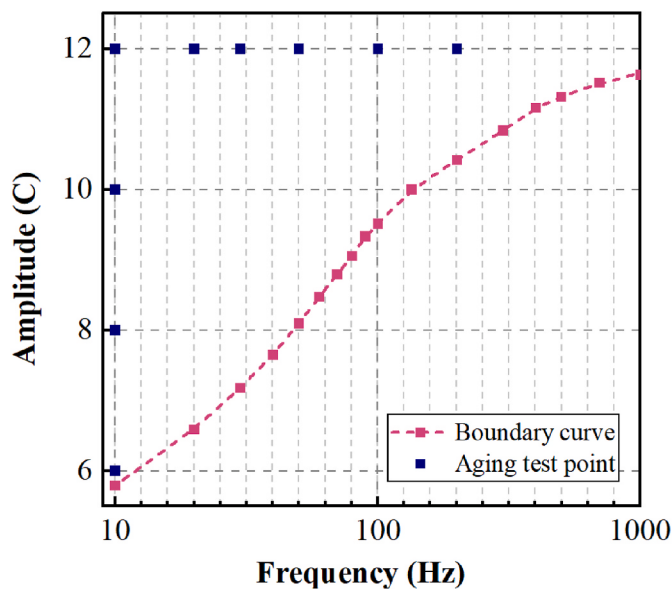


Fig. 2. The temperature rise boundary curve was fitted by the experiment, and the aging experimental points satisfying the temperature rise target were selected.

part of the impedance to frequency significantly weakens. At low-temperature, high-rate charging and discharging below 10 Hz can easily trigger battery aging, the frequency range was set from 10 to 1000 Hz. This experiment employed a logarithmic scale for frequency selection with an amplitude precision set at 0.1 A to conduct the temperature rise experiments and plot the temperature rise boundary curves.

2.3. Aging tests and disassembly experiment

2.3.1. Capacity and impedance calibration experiment

In this study, AC pulse self-heating was paused every five times to conduct a calibration experiment. The calibration experiment includes capacity test and EIS test. (1) Capacity test: the battery was charged at a CC of 0.5C (C-rate is the measurement of the charge and discharge current with respect to its nominal capacity) until the voltage reached to 3.65 V, followed by a CV charge at 3.65 V until the current was dropped below 0.05C. After resting for 1 h, the battery was discharged at 0.5C to 2 V. The cycle was repeated three times with the discharge capacity of the third cycle being considered to be the residual capacity of the battery; and (2) EIS test: the EIS mode adopts “EIS at open circuit potential”, measuring 5 different SOCs (10 %, 30 %, 50 %, 70 %, and 90 %) with a voltage amplitude of 5 mV and a frequency range of 100 kHz to 10 mHz. Following every five times of low-temperature self-heating, all batteries were rested for 2 h in the temperature test chamber to ensure a temperature of 25 °C for testing. For each experimental condition, two batteries were used to assess the reproducibility of the experiment.

2.3.2. Battery disassembly experiments

To observe the situation inside the aged batteries, the battery was disassembled after 30 self-heating cycles at 12 C and 10 Hz. Before disassembling, the battery was discharged at a CC of 0.5C to a cutoff voltage of 2 V. After resting for 5 min, the battery was discharged again at a CC of 0.05C–2 V to ensure that the battery was completely discharged. Finally, left the battery for over 3 h to reduce its safety risk. The steel shell of the aged battery was dismantled in the glove box filled with argon, where the concentrations of O₂ and H₂O were maintained below 0.01 ppm. Then the jelly roll formed by the electrode and separator was carefully separated. Simultaneously, cross contamination between the electrodes had to be avoided. Photographs of the graphite anode and LFP

cathode surfaces of batteries were taken inside the glove box to study the changes on the electrode surfaces.

3. Results and discussion

3.1. Influence of AC parameters on temperature rise

For temperature measurement, thermocouples were placed at the upper, middle, and lower positions of the battery surface. The temperature rise results of the battery at three positions under different AC parameters is shown in Fig. S3. As shown in Figs. S3(b–d), according to Joule's law, the larger the AC amplitude at the same frequency, the faster the battery temperature rise. Similarly, according to Fig. 1, as the AC frequency decreases, the real part of battery impedance increases, resulting in a faster temperature rise of the battery, so it shows the trend in Figs. S3(b–d). In addition, it can be seen from Fig. S3 that the temperature rise of the three positions of the battery is almost the same, with the temperature rise in the middle position slightly higher than that at the end position, which may be due to the more obvious heat loss at the end position of the battery. Therefore, in this study, the non-uniformity of battery temperature was ignored, and the average values of the obtained measurement data were taken as the final temperature.

Subsequently, the temperature rise boundary was found through experimental methods. The experimental data obtained are shown in Supplementary Table S1, and the typical temperature rise curves are shown in Fig. S4. To ensure the accuracy of the data, it is vital to have multiple data points around the final temperature of 0 °C. In this regard, a linear correction method is employed to adjust the amplitude of the final temperature of 0 °C to find the exact AC pulse parameters. Fig. 2 illustrates the boundary curve for the temperature rise of the battery from –20 °C to 0 °C under AC pulse experimental conditions. The red squares in the figure denote the data points adjusted based on the experiments, while the dashed lines represent the fitted boundary lines. The area above the dashed line indicates that heating the battery with these parameters can make the temperature rise exceed 0 °C, satisfying the requirements for temperature rise, and the farther away from the boundary, the higher the temperature rise; whereas, the area below the dashed line indicates that the temperature cannot reach 0 °C within 5 min, and the farther away from the boundary, the lower the temperature rise. The “steep-then-gentle” rising tendency of the temperature rise boundary curve corroborates with the heating theory of the thermo-electric coupling model [36], that is, under fixed amplitude conditions, the heat generation is primarily influenced by the real part of the battery impedance.

3.2. Aging analysis of self-heating

3.2.1. Effect of AC pulse amplitude and frequency on battery degradation

In the exploration of temperature rise boundaries during battery heating processes, it was observed that due to the differences in heating strategies, some batteries were unable to restore the open-circuit voltage to the initial value even after a day of rest following self-heating. Therefore, in the area above the boundary (Fig. 2), four longitudinal experimental points with the same frequency were chosen: 6 C 10 Hz, 8 C 10 Hz, 10 C 10 Hz, and 12 C 10 Hz, respectively, to investigate the impact of different amplitudes on the battery aging process. The combinations of 12 C amplitude and all frequency satisfied the temperature rise requirements. Therefore, six lateral experimental points with the same amplitude were selected: 12 C 10 Hz, 12 C 20 Hz, 12 C 30 Hz, 12 C 50 Hz, 12 C 100 Hz, and 12 C 200 Hz, respectively, to analyze the effect of frequency on battery aging during multiple self-heating processes.

After 30 times self-heating, the remaining capacity retention of the battery was plotted with the change of the times of self-heating. Fig. 3(a) illustrates the impact of different amplitudes on capacity retention under fixed frequency. The capacities of the batteries under all test conditions exhibit approximately linear declines. The greater the

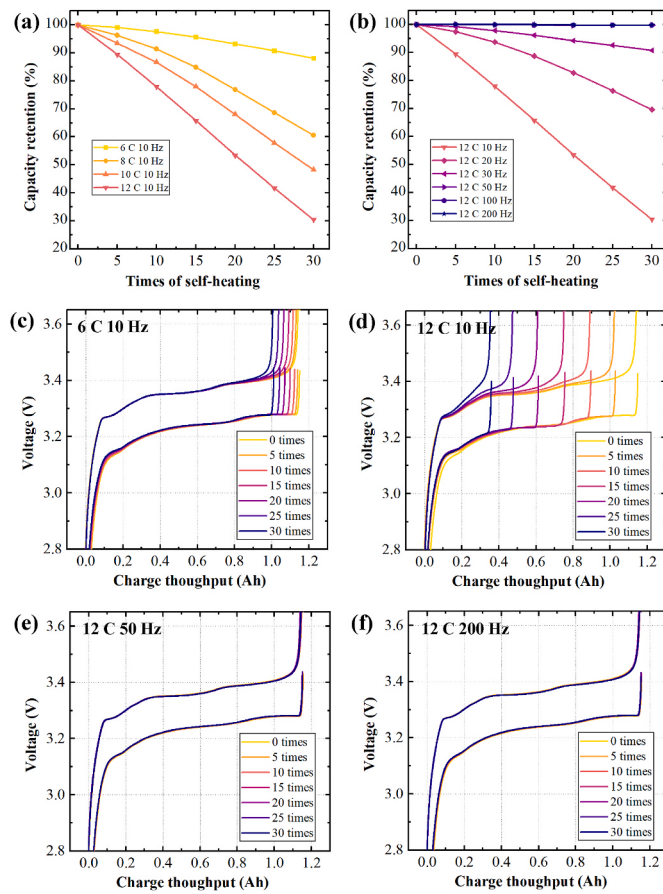


Fig. 3. Effect of AC pulse amplitude and frequency on battery degradation: the capacity retention under different (a) amplitudes and (b) frequency, voltage profile under (c) 6 C 10 Hz, (d) 12 C 10 Hz, (e) 12 C 50 Hz, and (f) 12 C 200 Hz with the times of self-heating.

amplitude, the lower the capacity retention rate. Specifically, the battery under 12 C and 10 Hz only maintains 30.4 % of its capacity after 30 times self-heating without any inflection point observed. Additionally, as shown in Fig. 3(b), when studying the effect of frequency on capacity retention at an amplitude of 12 C, it can be found that under the frequency conditions of 10 Hz, 20 Hz, and 30 Hz, the batteries similarly demonstrate almost linear decreases in capacities. However, when the frequency reaches or exceed 50 Hz, the battery capacity retention rate exhibits slight fluctuations at 100 %, which is considered a normal phenomenon. This indicates that self-heating at high frequencies has no impact on the State of Health (SOH) of battery.

Fig. 3(c–f) shows the distribution of the 0.5C charge-discharge voltages under four different self-heating conditions. It can be found that with increasing the times of self-heating, the high-voltage plateau of the battery shows a clear degradation, while the rest of the voltage distribution remains relatively stable. However, for the batteries at 12 C 50 Hz and 12 C 200 Hz, no changes can be observed in the 0.5C charge-discharge voltage curves. Additionally, for all nine self-heating conditions are shown in Fig. S5.

3.2.2. Nyquist plots during self-heating

To analyze the reasons for the decline in battery capacity retention, EIS testing technique was employed in this work. This method allows for the accurate identification of changes in the electrochemical performance of the battery without causing damage. The electrochemical workstation monitors the EIS information of the battery under different SOC. Fig. S6 shows the full-frequency domain electrochemical impedance variations with SOC. The changes of Nyquist plots at 50 % SOC

with the times of self-heating for self-heating conditions are shown in Fig. S7, revealing that the degree of curve shift is closely related to the SOH of battery. Fig. 4 display the Nyquist plots at 50 % SOC for batteries at 6 C 10 Hz, 12 C 10 Hz, 12 C 50 Hz, and 12 C 200 Hz, respectively, with the increase in the times of self-heating. For battery at 6 C 10 Hz and 12 C 10 Hz, the curves shift rightward with increasing the times of self-heating; whereas, for battery at 12 C 50 Hz and 12 C 200 Hz, a trend of leftward fluctuation at the curve inflection point with the increasing the times of self-heating can be observed.

3.2.3. Validation and preprocessing of EIS data

Before using the DRT method, the test data of EIS need to be validated first. The LIBs in this batch were examined using the Kramers-Kronig (K-K) relations for reconstructing the battery impedance spectra through a composite computational approach. The validity of the experimental data was done by ensuring that the relative error between the measured values and the K-K reconstructed impedance spectroscopy was maintained within 1 %. As shown in Fig. S8(a), for the fresh battery Cell 1, both the real and imaginary parts of the error are controlled within 1 %, indicating that the testing system satisfies the fundamental requirements of linearity, causality, and stability. Fig. S8 (b) illustrates the full-frequency domain K-K reconstructed impedance spectroscopy of the fresh battery Cell 1 at 50 % SOC. Consequently, the impedance data validated through the K-K relations can be employed for subsequent DRT peak analysis.

In the implementation of the DRT approach, this paper employed the Tikhonov regularization method [27,37] to deconvolute the EIS data. A Gaussian function was chosen as the base function, and the Lambda coefficient (set at 1E-06) was adjusted to balance the smoothness and resolution of the DRT results, ensuring that the Sum of Squared Residuals (SSR) between preprocessing and signal reproduction remained minimal. The computational results for different frequency intervals are shown in Fig. S9. For the high-frequency phase in DRT, the existing research has demonstrated the efficacy of these data in identifying contact impedance (including the impedance between active material particles and between active materials and current collectors) [38–41]. For the low-frequency diffusion phase in DRT analysis, it can be found that it has no effect on the high-frequency calculation results. The results are only estimative due to non-convergence of the low frequency phase computation. Nevertheless, the time constant marking the beginning of the diffusion region can still be identified in the DRT plot. To ensure no critical information is overlooked, it is appropriate to choose a frequency range of 0.1 Hz–10 kHz for DRT analysis. The process of preprocessing EIS data and its reproduction with DRT is shown in Fig. S8(c).

3.2.4. DRT partitioning

Fig. S10(a) displays DRT results of the fresh battery Cell 1 at 25 °C under five different SOC conditions, where four domains can be identified, represented as A₁-A₄, each representing an individual polarization process. Among them, the SOC dependency of A₁ and A₂ can be neglected; while A₃ and A₄ are closely related to SOC, the peak area decreases with the increase of SOC. By calculating different frequency ranges of DRT in the early stage, A₄ can be associated with diffusion impedance.

Fig. S10(b) shows the DRT results at five different temperatures under 50 % SOC. All areas from A₁-A₄ are temperature-dependent, and the polarization impedance significantly increases as the temperature decreases. Compared A₁ with A₂, A₁ is much less sensitive to temperature, and thus, A₁ is attributed to the contact resistance R_c. The impedance response of 18650 graphite||LFP battery in the mid-frequency area of EIS has been confirmed, with the higher frequency domain being solid electrolyte interphase (SEI) impedance, and the lower frequency domain being charge transfer impedance [42]. It can be found that A₂ is almost independent of SOC, while A₃ depends on SOC. Considering this difference, A₂ and A₃ are identified as the SEI impedance, denoted as R_{sei}, and the charge transfer reaction impedance,

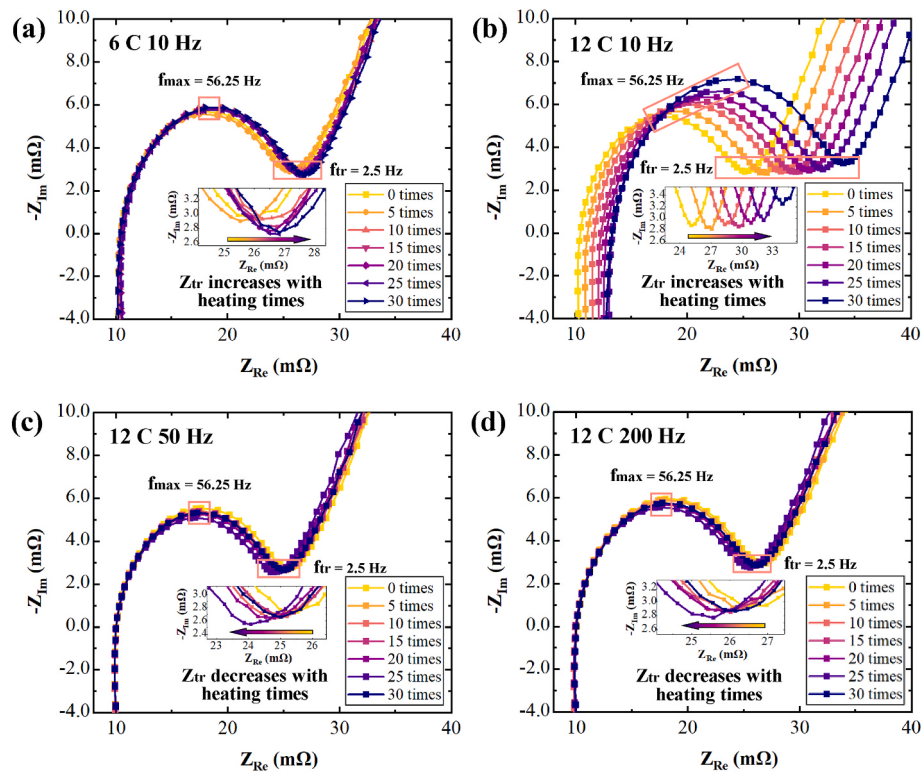


Fig. 4. Nyquist plots of batteries with different aging conditions at 50 % SOC with the times of self-heating: (a) 6 C 10 Hz, (b) 12 C 10 Hz, (c) 12 C 50 Hz, (d) 12 C 200 Hz.

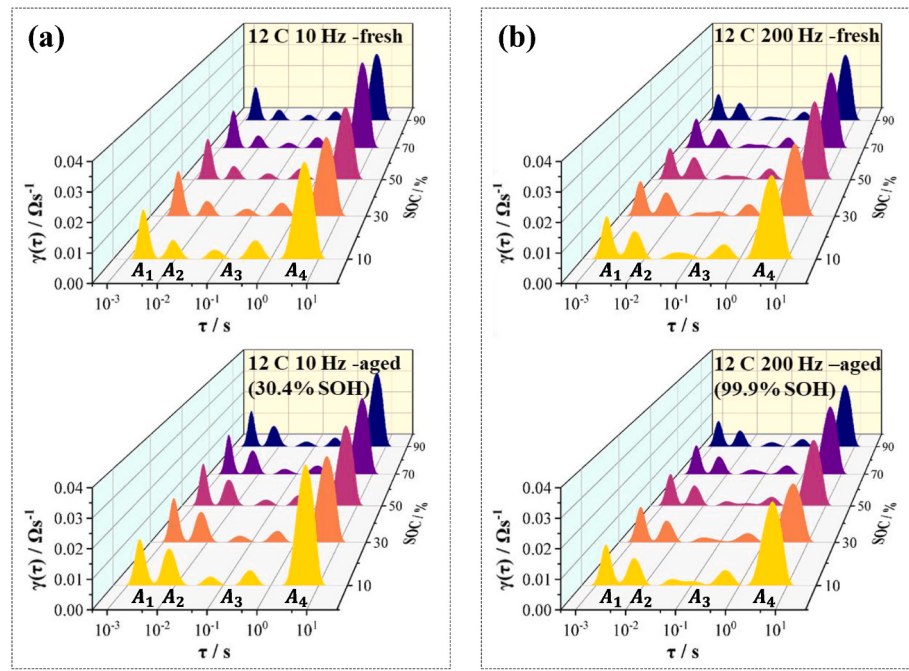


Fig. 5. DRT results of EIS data measured under different aging conditions: (a) 12 C 10 Hz, (b) 12 C 200 Hz.

denoted as R_{ct} , respectively. Moreover, A₃ contains two peaks, which may be related to multiple interface reactions. Such a division of domain has also been confirmed in previous literature [40,43].

The value of R_{o} is equal to the Z_{Re} when the Z_{Im} is zero, and other impedances are calculated through the integration of the domain. As shown in Fig. S11, the impedance within the temperature range of -10 to 25 °C obeys the Arrhenius relation with the reciprocal of absolute

temperature.

3.2.5. Analysis of degradation mechanisms through the DRT method

Fig. 5 displays the results of DRT analysis for the battery under 12 C 10 Hz and 12 C 200 Hz, with the results under other conditions available in Fig. S12. Two pictures in this figure correspond to the DRT results before and after 30 times self-heating, respectively. The most noticeable

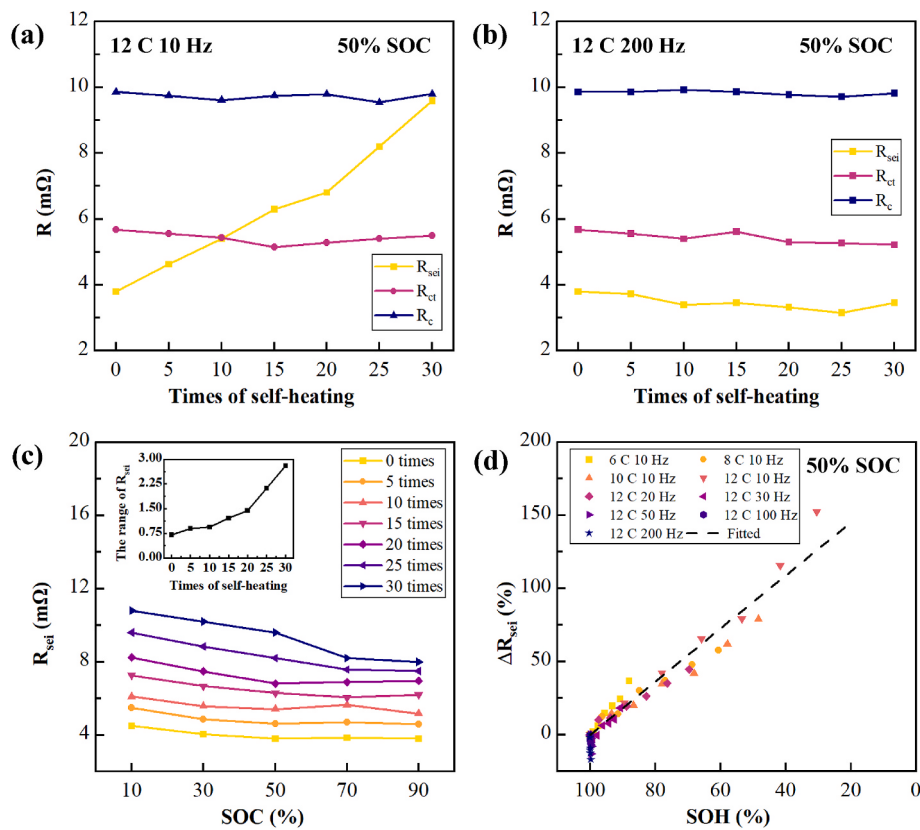


Fig. 6. Integral result of DRT: polarization impedance of battery at 50 % SOC under (a) 12 C 10 Hz and (b) 12 C 200 Hz, (c) R_{sei} of battery under 12 C 10 Hz at different SOCs with the times of self-heating, (d) ΔR_{sei} vs. SOH under all AC pulse conditions.

change in the DRT results is in the domain A₂, which is impacted by R_{sei} .

According to the division of the domain in Section 3.2.4, the polarization impedance can be obtained by integrating over the corresponding time constant range for each domain. Fig. 6(a) shows the variation of each polarization impedance for battery under 12 C 10 Hz at 50 % SOC. It is observed that R_{sei} increases with increasing the times of self-heating, reaching 2.53 times its original value after heating 30 times. In contrast, R_c and R_{ct} exhibit relatively minor changes throughout the self-heating process, fluctuating within a certain range. Therefore, for LIB after aging due to AC pulse self-heating, the increase in impedance is primarily dominated by R_{sei} .

The polarization impedances of the battery under 12 C 200 Hz at 50 % SOC obtained through DRT integration are shown in Fig. 6(b). The impedances R_c , R_{ct} , and R_{sei} show minimal changes throughout the entire self-heating process of 30 times. Slight decrease of R_{ct} and R_{sei} can be observed, confirming that appropriate high-rate and high-frequency cycling have a positive impact on reducing the impedance of LIB. Additionally, Fig. 6(c) shows the plot the R_{sei} of battery under 12 C 10 Hz at different SOCs with the times of self-heating. An increasing trend of R_{sei} with increasing the times of self-heating can be observed, indicating that R_{sei} will increase when the battery SOH decreases. The $(\max - \min)R_{sei}$ is defined as the range of R_{sei} at different SOCs in the same SOH. With increasing the times of self-heating, the battery SOH decreases so that the range of R_{sei} increases, indicating an exacerbation in battery capacity degradation, and the increased instability under different SOCs.

The relative variations of R_{sei} in the self-heating process of the batteries under all experimental conditions are summarized. As shown in Fig. 6(d), the trend of ΔR_{sei} change is closely related to the battery SOH, indicating that ΔR_{sei} can serve as a significant index for evaluating the change of SOH during the self-heating process of the battery. When the amplitude is 12 C and the frequency is 50 Hz, 100 Hz, and 200 Hz, the

R_{sei} decreases slightly, indicating that after AC pulse with large amplitude and high frequency, the battery performance has been improved.

To further determine the degradation mechanism, the battery heated 30 times at -20°C with 12 C 10 Hz AC pulse is completely discharged and disassembled to characterize its morphology. Compared with the fresh battery, there is no significant change in the LFP cathode of the aged battery (Fig. S13), but the aged graphite anode is obviously plated with a large amount of lithium metal (Fig. 7(a)). When the aged graphite anode is exposed to air for a few minutes, the lithium metal layer reacts with the air to form the white oxide (Fig. 7(b)). According to the scanning electron microscope (SEM) images, the outlines of fresh graphite anode particles are clearly visible (Fig. 7(c)), but the surface of the aged graphite anode is uniformly plated with a large amount of metal lithium, even causing the graphite particles to be unobservable (Fig. 7(d)). The energy dispersive spectrometer (EDS) images of the aged graphite anode show that the covering layer is mainly composed of metal lithium oxide (Fig. 7(e)), while the uncovered areas are graphite (Fig. 7(f)). It is due to the reaction between the plated lithium metal and oxygen during the detection process to form oxides.

The lithium plating is closely related to the anode potential. When the AC pulse condition causes the anode potential to be lower than 0 V (vs. Li/Li⁺) [44,45], lithium plating occurs. After lithium plating at low temperatures, the increase in R_{sei} can be explained by several aspects [46]: a part of the lithium metal may react with the electrolyte to recombine and form a thicker and more complex SEI; a part of the lithium metal may protrude outside the SEI, causing delamination of the SEI from graphite; moreover, lithium metal may impede the movement of lithium ions through the SEI. Notably, even when the lithium plating is very severe, no additional lithium layer peaks can be observed in the DRT, indicating that the lithium plating layer is not completely dense, but on a microscopic scale, the deposition of lithium metal only increases the transport distance of lithium ions to the graphite surface,

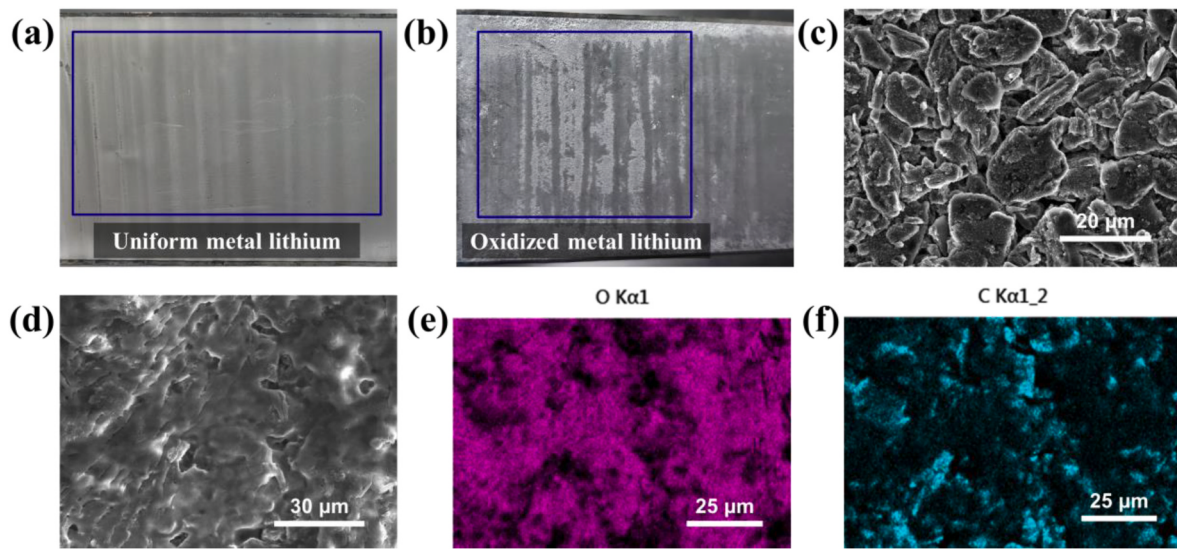


Fig. 7. Characterization of aged anode (30.4 % SOH) after disassembling: (a) photo of the aged anode plated with a large amount of metal lithium, (b) photo of oxidized metal lithium on the surface of the aged anode, (c) SEM image of the fresh anode surface, (d) SEM image of the aged anode surface, (e) EDS image of oxygen distribution in Fig. (d), (f) EDS image of carbon distribution in Fig. (d).

thereby making the SEI more resistive.

3.3. Analysis of self-heating based on electrochemical model

Based on results of the aging analysis presented in Section 3.2, an ETC model incorporating the lithium plating side reaction has been developed. The pseudo-two-dimensional (P2D) model developed by Doyle and Newman, also known as the electrochemical model of battery, can accurately simulate the charging and discharging response of the batteries. In this study, the ETC model was established by coupling a heat transfer model based on the P2D model, and additionally the lithium plating current density and double layer current density were calculated to simulate the temperature rise and aging process of the battery under AC pulse self-heating. The following only shows the key equations of the ETC model. Other governing equations are given in Supplementary Note 1, and the electrochemical and thermal parameters of the model are listed in the Supplementary Table S3. Moreover, the experimental verification results of the model are shown in Fig. S14.

The traditional P2D model is established under the isothermal assumption. To calculate the temperature variation of the battery, the Arrhenius equation is normally used to couple temperature and electrochemical parameters [33], as shown in Eq. (1). The temperature of batteries is calculated using the energy conservation equation, as shown in Eq. (2).

$$R_{\text{Arrhe}} = \exp \left[\frac{E_a}{R} \left(\frac{1}{T_r} - \frac{1}{T} \right) \right] \quad (1)$$

$$\rho c_p \frac{\partial T}{\partial t} = q_J - hA(T - T_{\text{env}}) \quad (2)$$

where R_{Arrhe} is the temperature correction coefficient, E_a is the activation energy of the electrochemical parameter, T_r is the reference temperature, T is the battery temperature, ρ represents battery density, c_p is the specific heat capacity of the battery, q_J denotes the total heat source, h is the convective heat transfer coefficient between the battery and the environment, A is the specific surface area of the battery, and T_{env} stands for the environmental temperature.

Under low-temperature AC conditions, the lithium plating reaction on the graphite anode surface is the primary cause of battery capacity degradation. This process can be described using the Butler-Volmer equation [47]. The current density for the lithium plating reaction is

shown in Eq. (3).

$$j_p = k_p c_e^{\alpha_p} \left[\exp \left(\frac{\alpha_p \phi_p F}{RT} \right) - \exp \left(\frac{(1 - \alpha_p) \phi_p F}{RT} \right) \right] \quad (3)$$

where j_p is the current density of lithium plating, k_p is the reaction rate constant of lithium plating, c_e is the lithium ion concentration in the electrolyte, α_p is the anode transfer coefficient, ϕ_p is the reaction overpotential of lithium plating, F is the Faraday's constant, and R is the gas constant.

When the direction of the applied current in the battery frequently changes, it is necessary to consider the double layer current resulting from the charge redistribution process at the electrode/electrolyte interface [48]. The total local current density j_s at the electrode/electrolyte interface includes both Faraday current density j_f and non-Faraday current density j_{nf} . The Faraday current density is related to the redox reactions at the electrode/electrolyte interface, such as the lithium-ion intercalation/deintercalation reactions and the lithium plating reaction at the graphite anode. In contrast, the non-Faraday current density arises from the double layer capacitance effect, which does not involve redox reactions. After ignoring the concentration dependence of the double layer charging and discharging current, the double layer current density can be represented by Eq. (4).

$$j_{dl} = \frac{C_{dl}}{F} \frac{\partial \phi_{dl}}{\partial t} \quad (4)$$

where j_{dl} is the current density of the double layer, C_{dl} is the double layer capacitance, and ϕ_{dl} is the double layer potential.

Consequently, the total local current density at the graphite anode surface can be expressed by Eq. (5). It can be found that the electrochemical reactions on the electrode surface will be affected due to the double layer. In contrast, at the LFP cathode surface, only lithium-ion intercalation/deintercalation reactions and the double layer exist.

$$j_s = j_f + j_{nf} = j_i + j_p + j_{dl} \quad (5)$$

where j_s is the total local current density, j_f is the Faraday current density, j_{nf} is the non-Faraday current density, and j_i is the current density for lithium-ion intercalation/deintercalation reaction.

To determine AC pulse parameters that simultaneously satisfy temperature rise requirements without capacity loss, the ETC model is used to explore the entire AC pulse parameter space. The computed AC pulse

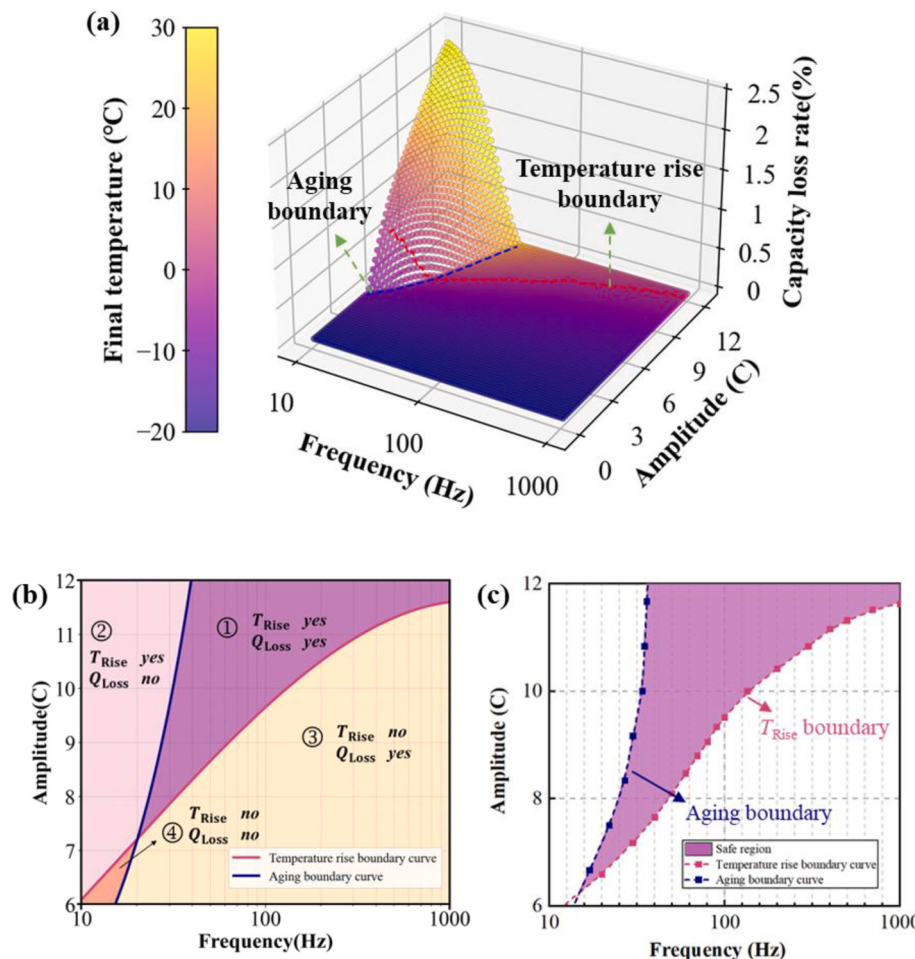


Fig. 8. Temperature rise and capacity loss under different AC pulse amplitude and frequency: (a) 4-D relationship chart of frequency, amplitude, final temperature and capacity loss rate after 5 min of AC pulse self-heating, aging boundary and temperature rise boundary from (b) model and (c) experiment.

amplitude and frequency in relation to battery final temperature and capacity loss are illustrated in a 4D cloud mapping, as shown in Fig. 8(a). In the figure, the red line represents the AC pulse parameters capable of heating the battery to 0 °C, namely the temperature rise boundary. The blue line signifies the AC pulse parameters that just avoid capacity loss, namely the aging boundary. To the left of the aging boundary, $Q_{Loss} > 0$, and the farther from the boundary, the larger the Q_{Loss} . To the right of the aging boundary, $Q_{Loss} = 0$. It is evident that under most AC pulse parameters, high temperature rise and low capacity loss are contradictory. Only using the AC pulse parameters composed of high frequencies and high amplitudes can satisfy both of these requirements simultaneously.

Based on the computational results of the model, the boundaries of temperature rise and aging within the AC pulse parameter space are plotted, as shown in Fig. 8(b). Correspondingly, the aging boundary is also explored through experiments. Based on the aging analysis results presented in Section 3.2.1, it can be found that the battery capacity exhibits a near-linear decline with increasing the times of self-heating. Therefore, in this paper, the condition for battery aging is defined as follows: the capacity test conducted at 25 °C results in a capacity change controlled within ± 3 mAh compared to the initial capacity before self-heating, equivalent to an allowable relative capacity change range of $\pm 0.3\%$. Such a definition allows for a more accurate determination of the battery's aging state. In the process of identifying aging boundaries, the frequency is divided into ten equal parts on a logarithmic scale, with an amplitude accuracy of 1 A. To avoid the phenomenon of inconspicuous capacity degradation due to insufficient times of self-heating of the

battery, the times of self-heating for all batteries in this experiment was uniformly set to 8. For each experimental point, two batteries were used to conduct repetitive experiments to ensure the reliability of the aging boundaries. The experimental data were recorded in Table S2. The boundaries of temperature rise and aging, as drawn from the experimental results, are presented in Fig. 8(c). It can be observed that the simulation results are in good agreement with the experimental outcomes. These boundaries divide the AC pulse parameter space into four distinct domains. Domain 1 represents the optimal heating domain that satisfies the requirements for temperature rise while avoiding battery aging. Utilizing the self-heating parameters of this domain not only rapidly increases the battery temperature but also does not compromise battery life. Therefore, the established ETC model that can simultaneously calculate battery temperature rise and capacity loss not only confirms the aging analysis results of DRT, but also provides an effective solution for quickly determining the optimal heating domain for battery self-heating.

4. Conclusions

This paper focusing on the aging behavior of LIBs during the low-temperature AC pulse self-heating, the aging process of batteries is monitored by applying quantitative DRT analysis method to identify the fundamental causes of battery capacity degradation. Subsequently, an ETC model is developed based on the battery degradation mechanism to determine the optimal heating domain for LIBs under AC pulse self-heating conditions through integrating theoretical models with

experimental results. The findings indicate that at an AC pulse frequency of 50 Hz or higher, there is no degradation for the battery used in this study even with an amplitude of up to 12 C. According to DRT analysis, the increase in SEI impedance caused by lithium plating is the primary aging reason when inappropriate frequencies and amplitudes are selected during the AC pulse self-heating. Moreover, conducting charging and discharging with high amplitude and frequency is found to reduce the impedance of unaged batteries, thereby extending battery life. Finally, the ETC model established based on aging analysis results can accurately simulate battery behavior under AC pulse self-heating in low-temperature environments and effectively predict the optimal heating domain for battery self-heating. The results show that only high-frequency and high-amplitude AC pulse parameters could heat the battery to above 0 °C within 5 min without capacity loss.

The primary contribution of this research is to uncover the battery aging cause during the AC pulse self-heating. This insight provides a theoretical foundation for designing more effective battery heating strategies. In the future work, we will develop a safer and faster self-heating strategy by considering the safety cut-off voltage and lithium plating current boundary as optimization targets. Furthermore, we will also conduct more in-depth research on other aging mechanisms of batteries under AC self-heating through the ETC model.

CRediT authorship contribution statement

Zixian Zhuang: Writing – review & editing, Writing – original draft, Visualization, Software, Methodology, Investigation, Data curation, Conceptualization. **Jun Li:** Writing – original draft, Visualization, Software, Data curation. **Weiling Luan:** Writing – review & editing, Supervision, Project administration. **Haofeng Chen:** Writing – review & editing, Resources, Investigation. **Qiu-An Huang:** Writing – review & editing, Validation. **Jiujun Zhang:** Writing – review & editing. **Shantung Tu:** Writing – review & editing.

Declaration of competing interest

The authors declare that they have no known competing financial interests or personal relationships that could have appeared to influence the work reported in this paper.

Data availability

No data was used for the research described in the article.

Acknowledgements

The authors gratefully acknowledge the support from the National Natural Science Foundation of China (52375144, 52150710540 and 52375145) and the East China University of Science and Technology, University of Strathclyde, Shanghai University during the course of this work.

Appendix A. Supplementary data

Supplementary data to this article can be found online at <https://doi.org/10.1016/j.jpowsour.2024.235442>.

References

- [1] J. Xing, S. Bliznakov, L. Bonville, et al., A review of nonaqueous electrolytes, binders, and separators for lithium-ion batteries, *Electrochim. Energy Rev.* 5 (4) (2022) 14, <https://doi.org/10.1007/s41918-022-00131-z>.
- [2] Q. Meng, S. Lou, B. Shen, et al., Reevaluating flexible lithium-ion batteries from the insights of mechanics and electrochemistry, *Electrochim. Energy Rev.* 5 (SUPPL 2) (2022) 30, <https://doi.org/10.1007/s41918-022-00150-w>.
- [3] J. Song, H. Wang, Y. Zuo, et al., Building better full manganese-based cathode materials for next-generation lithium-ion batteries, *Electrochim. Energy Rev.* 6 (1) (2023) 20, <https://doi.org/10.1007/s41918-023-00184-8>.
- [4] Y. Wang, X. Zhang, K. Li, et al., Perspectives and challenges for future lithium-ion battery control and management, *eTransportation* 18 (2023) 100260, <https://doi.org/10.1016/j.etrans.2023.100260>.
- [5] N. Piao, X. Gao, H. Yang, et al., Challenges and development of lithium-ion batteries for low temperature environments, *eTransportation* 11 (2022) 100145, <https://doi.org/10.1016/j.etrans.2021.100145>.
- [6] S. Wu, C. Wang, W. Luan, et al., Thermal runaway behaviors of Li-ion batteries after low temperature aging: experimental study and predictive modeling, *J. Energy Storage* 66 (2023) 107451, <https://doi.org/10.1016/j.est.2023.107451>.
- [7] A. Senyshyn, M.J. Mühlbauer, O. Dolotko, et al., Low-temperature performance of Li-ion batteries: the behavior of lithiated graphite, *J. Power Sources* 282 (2015) 235–240, <https://doi.org/10.1016/j.jpowsour.2015.02.008>.
- [8] T. Sun, T. Shen, Y. Zheng, et al., Modeling the inhomogeneous lithium plating in lithium-ion batteries induced by non-uniform temperature distribution, *Electrochim. Acta* 425 (2022) 140701, <https://doi.org/10.1016/j.electacta.2022.140701>.
- [9] V. Talele, U. Morali, H.N. Khobshan, et al., Improving battery safety by utilizing composite phase change material to delay the occurrence of thermal runaway event, *Int. Commun. Heat Mass Tran.* 155 (2024) 107527, <https://doi.org/10.1016/j.icheatmastransfer.2024.107527>.
- [10] Pu J, Ping XF, Panchal S, et al. Structural optimization of a serpentine-channel cold plate for thermal management of lithium-ion battery based on the field synergy principle. Available at SSRN 2024:4795285. <https://doi.org/10.2139/ssrn.4795285>.
- [11] A.H. Vakilzadeh, A.B. Sarvestani, K. Javaherdeh, et al., Heat transfer and fluid flow in a PCM-filled enclosure: effect of heated wall configuration, *J. Energy Storage* 87 (2024) 111448, <https://doi.org/10.1016/j.est.2024.111448>.
- [12] H.N. Khobshan, F. Jalilintabar, A.A. Abdullah, et al., Parametric investigation of battery thermal management system with phase change material, metal foam, and fins; utilizing CFD and ANN models, *Appl. Therm. Eng.* 247 (2024) 123080, <https://doi.org/10.1016/j.aplthermaleng.2024.123080>.
- [13] A. Kvasha, C. Gutierrez, U. Osa, et al., A comparative study of thermal runaway of commercial lithium ion cells, *Energy* 159 (2018) 547–557, <https://doi.org/10.1016/j.energy.2018.06.173>.
- [14] K. Shah, C. McKee, D. Chalise, et al., Experimental and numerical investigation of core cooling of Li-ion cells using heat pipes, *Energy* 113 (2016) 852–860, <https://doi.org/10.1016/j.energy.2016.07.076>.
- [15] Q. Wang, B. Jiang, B. Li, et al., A critical review of thermal management models and solutions of lithium-ion batteries for the development of pure electric vehicles, *Renew. Sustain. Energy Rev.* 64 (2016) 106–128, <https://doi.org/10.1016/j.rser.2016.05.033>.
- [16] C.-Y. Wang, G. Zhang, S. Ge, et al., Lithium-ion battery structure that self-heats at low temperatures, *Nature* 529 (7587) (2016) 515–518, <https://doi.org/10.1038/nature16502>.
- [17] J. Li, D. Sun, Lithium-ion batteries modeling and optimization strategies for sinusoidal alternating current heating at low temperature, *Energy Proc.* 152 (2018) 562–567, <https://doi.org/10.1016/j.egypro.2018.09.211>.
- [18] Z.G. Qu, Z.Y. Jiang, Q. Wang, Experimental study on pulse self-heating of lithium-ion battery at low temperature, *Int. J. Heat Mass Tran.* 135 (2019) 696–705, <https://doi.org/10.1016/j.ijheatmastransfer.2019.02.020>.
- [19] J. Zhu, Z. Sun, X. Wei, et al., Experimental investigations of an AC pulse heating method for vehicular high power lithium-ion batteries at subzero temperatures, *J. Power Sources* 367 (2017) 145–157, <https://doi.org/10.1016/j.jpowsour.2017.09.063>.
- [20] H. Ruan, J.V. Barreras, M. Steinhardt, et al., The heating triangle: a quantitative review of self-heating methods for lithium-ion batteries at low temperatures, *J. Power Sources* 581 (2023) 233484, <https://doi.org/10.1016/j.jpowsour.2023.233484>.
- [21] J. Zhang, H. Ge, Z. Li, et al., Internal heating of lithium-ion batteries using alternating current based on the heat generation model in frequency domain, *J. Power Sources* 273 (2015) 1030–1037, <https://doi.org/10.1016/j.jpowsour.2014.09.181>.
- [22] J. Zhu, Z. Sun, X. Wei, et al., Experimental investigations of an ac pulse heating method for vehicular high power lithium-ion batteries at subzero temperatures, *J. Power Sources* 367 (2017) 145–157, <https://doi.org/10.1016/j.jpowsour.2017.09.063>.
- [23] X. Wang, X. Wei, J. Zhu, et al., A review of modeling, acquisition, and application of lithium-ion battery impedance for onboard battery management, *eTransportation* 7 (2021) 100093, <https://doi.org/10.1016/j.etrans.2020.100093>.
- [24] F. Cai, S. Cai, Z. Tu, Proton exchange membrane fuel cell (PEMFC) operation in high current density (HCD): problem, progress and perspective, *Energy Convers. Manag.* 307 (2024) 118348, <https://doi.org/10.1016/j.enconman.2024.118348>.
- [25] J. Lv, Z. Yu, G. Sun, et al., Deep learning-based fault diagnosis and electrochemical impedance spectroscopy frequency selection method for proton exchange membrane fuel cell, *J. Power Sources* 591 (2024) 233815, <https://doi.org/10.1016/j.jpowsour.2023.233815>.
- [26] Y. Bai, Q.-A. Huang, K. Wu, et al., Decouple charge transfer reactions in the Li-ion battery, *J. Energy Chem.* 92 (2024) 759–798, <https://doi.org/10.1016/j.jecchem.2024.02.003>.
- [27] Y. Lu, C.-Z. Zhao, J.-Q. Huang, et al., The timescale identification decoupling complicated kinetic processes in lithium batteries, *Joule* 6 (6) (2022) 1172–1198, <https://doi.org/10.1016/j.joule.2022.05.005>.
- [28] M. Gaberscek, J. Moskon, B. Erjavec, et al., The importance of interphase contacts in Li ion electrodes: the meaning of the high-frequency impedance arc, *Electrochim. Solid State Lett.* 11 (10) (2008) A170–A174, <https://doi.org/10.1149/1.2964220>.

- [29] M. Steinhauer, S. Risse, N. Wagner, et al., Investigation of the solid electrolyte interphase formation at graphite anodes in lithium-ion batteries with electrochemical impedance spectroscopy, *Electrochim. Acta* 228 (2017) 652–658, <https://doi.org/10.1016/j.electacta.2017.01.128>.
- [30] C. Sheng, F. Yu, C. Li, et al., Diagnosing the SEI layer in a potassium ion battery using distribution of relaxation time, *J. Phys. Chem. Lett.* 12 (8) (2021) 2064–2071, <https://doi.org/10.1021/acs.jpclett.1c00118>.
- [31] L. Li, C. Fang, W. Wei, et al., Nano-ordered structure regulation in delithiated Si anode triggered by homogeneous and stable Li-ion diffusion at the interface, *Nano Energy* 72 (2020) 104651, <https://doi.org/10.1016/j.nanoen.2020.104651>.
- [32] J. Wang, R. Zhao, Q.-A. Huang, et al., High-efficient prediction of state of health for lithium-ion battery based on AC impedance feature tuned with Gaussian process regression, *J. Power Sources* 561 (2023) 232737, <https://doi.org/10.1016/j.jpowsour.2023.232737>.
- [33] D. Ren, K. Smith, D. Guo, et al., Investigation of lithium plating-stripping process in Li-ion batteries at low temperature using an electrochemical model, *J. Electrochem. Soc.* 165 (10) (2018) A2167–A2178, <https://doi.org/10.1149/2.0661810jes>.
- [34] X.-G. Yang, Y. Leng, G. Zhang, et al., Modeling of lithium plating induced aging of lithium-ion batteries: transition from linear to nonlinear aging, *J. Power Sources* 360 (2017) 28–40, <https://doi.org/10.1016/j.jpowsour.2017.05.110>.
- [35] T. Liu, X.-G. Yang, S. Ge, et al., Ultrafast charging of energy-dense lithium-ion batteries for urban air mobility, *eTransportation* 7 (2021) 100103, <https://doi.org/10.1016/j.etran.2021.100103>.
- [36] J. Li, D. Sun, Z. Chai, et al., Sinusoidal alternating current heating strategy and optimization of lithium-ion batteries with a thermo-electric coupled model, *Energy* 186 (2019) 115798, <https://doi.org/10.1016/j.energy.2019.07.128>.
- [37] T.H. Wan, M. Saccoccia, C. Chen, et al., Influence of the discretization methods on the distribution of relaxation times deconvolution: implementing radial basis functions with DRTtools, *Electrochim. Acta* 184 (2015) 483–499, <https://doi.org/10.1016/j.electacta.2015.09.097>.
- [38] Q. Zhang, D. Wang, E. Schatzl, et al., Degradation mechanism analysis and State-of-Health estimation for lithium-ion batteries based on distribution of relaxation times, *J. Energy Storage* 55 (2022) 105386, <https://doi.org/10.1016/j.est.2022.105386>.
- [39] R. He, Y. He, W. Xie, et al., Comparative analysis for commercial li-ion batteries degradation using the distribution of relaxation time method based on electrochemical impedance spectroscopy, *Energy* 263 (2023) 125972, <https://doi.org/10.1016/j.energy.2022.125972>.
- [40] X. Zhou, J. Huang, Z. Pan, et al., Impedance characterization of lithium-ion batteries aging under high-temperature cycling: importance of electrolyte-phase diffusion, *J. Power Sources* 426 (2019) 216–222, <https://doi.org/10.1016/j.jpowsour.2019.04.040>.
- [41] X. Zhou, Z. Pan, X. Han, et al., An easy-to-implement multi-point impedance technique for monitoring aging of lithium ion batteries, *J. Power Sources* 417 (2019) 188–192, <https://doi.org/10.1016/j.jpowsour.2018.11.087>.
- [42] B. Manikandan, V. Ramar, C. Yap, et al., Investigation of physico-chemical processes in lithium-ion batteries by deconvolution of electrochemical impedance spectra, *J. Power Sources* 361 (2017) 300–309, <https://doi.org/10.1016/j.jpowsour.2017.07.006>.
- [43] H. You, B. Jiang, J. Zhu, et al., In-situ quantitative detection of irreversible lithium plating within full-lifespan of lithium-ion batteries, *J. Power Sources* 564 (2023) 232892, <https://doi.org/10.1016/j.jpowsour.2023.232892>.
- [44] S. Tippmann, D. Walper, L. Balboa, et al., Low-temperature charging of lithium-ion cells part I: electrochemical modeling and experimental investigation of degradation behavior, *J. Power Sources* 252 (2014) 305–316, <https://doi.org/10.1016/j.jpowsour.2013.12.022>.
- [45] M. Doyle, T.F. Fuller, J. Newman, Modeling of galvanostatic charge and discharge of the lithium/polymer/insertion cell, *J. Electrochem. Soc.* 140 (6) (1993) 1526–1533, <https://doi.org/10.1149/1.2221597>.
- [46] D.E. Brown, E.J. McShane, Z.M. Konz, et al., Detecting onset of lithium plating during fast charging of Li-ion batteries using operando electrochemical impedance spectroscopy, *Cell Rep Phys Sci* 2 (10) (2021) 100589, <https://doi.org/10.1016/j.xrpp.2021.100589>.
- [47] P. Arora, M. Doyle, R.E. White, Mathematical modeling of the lithium deposition overcharge reaction in lithium-ion batteries using carbon-based negative electrodes, *J. Electrochem. Soc.* 146 (10) (1999) 3543–3553, <https://doi.org/10.1149/1.1392512>.
- [48] Q. Zhang, D. Wang, B. Yang, et al., Electrochemical model of lithium-ion battery for wide frequency range applications, *Electrochim. Acta* 343 (2020) 136094, <https://doi.org/10.1016/j.electacta.2020.136094>.